



*The 32nd International Congress and Exposition on Noise Control Engineering
Jeju International Convention Center, Seogwipo, Korea,
August 25-28, 2003*

[N355] Experimental and Numerical Study of Spatial Coherence of Surface Pressure on a Square Cylinder for Numerical Aerodynamic Noise Prediction

Takuya Oshima

*Department of Civil Engineering and Architecture, Faculty of Engineering, Niigata University
8050 Igarashi-Nincho, Niigata City, Japan 950-2181
oshima@eng.niigata-u.ac.jp*

Hidehisa Sekine and Michihito Terao

*Department of Architecture, Faculty of Engineering
Kanagawa University, Japan*

ABSTRACT

Aerodynamic noises from building exterior subsidiaries such as balusters or louver fins exposed to strong winds give serious psychological impact to inhabitants. To reduce required resources for three-dimensional aeroacoustic source computation of such two-dimensional bodies, an estimation method of full-span acoustic intensity from a partial-span computation has been formerly presented by one of the authors. The method has stood on an unproved assumption that the real part of complex coherence of surface pressure as function of spanwise distance obeys Gaussian function, which is examined experimentally and computationally in this investigation. The experiments are conducted in a low-noise wind tunnel using a square-cylindrical test body in which surface pressure sensors are embedded. In computations, a Large Eddy Simulation with the standard Smagorinsky model is employed. Reynolds numbers range from 4620 to 9240 and the angles of attack from 0 to 30 degrees. The results tell that in all cases the real parts of complex coherences fit well with Gaussian function especially at Kármán frequencies. Although coherent structures also agreed qualitatively between experiments and computations, large discrepancies are found in coherent lengths. The investigation of the cause remains as future work.

1 INTRODUCTION

Aerodynamic noises from building exterior subsidiaries such as balusters or louver fins exposed to strong winds give serious psychological impact to inhabitants. To reduce required resources for three-dimensional aeroacoustic source computation of such two-dimensional bodies, an estimation method of acoustic intensity radiated from full-span of the body using a result of partial-span computation has been formerly presented by one of the authors[2]. The method, however, has stood on an unproved assumption that the real part of spanwise averaged complex coherence of surface pressure as function of spanwise distance obeys Gaussian function. Thus the verification of the assumption through experiments and computations will be given in this investigation. Furthermore, comparison of experimental and computational results under the same Reynolds numbers will be attempted to examine overall effectiveness of numerical prediction.

2 EXPERIMENTAL SETUP AND NUMERICAL METHODS

2.1 Basic Theory

Aeroacoustic intensity at a certain frequency generated by interaction between flow and a cylindrical body is calculated using spanwise averaged coherence function as to complex amplitude of body surface as follows (see reference [2] for details).

$$\gamma(\xi) = \frac{1}{a - \xi} \int_{-a/2}^{a/2 - \xi} \mu(x_3, x_3 + \xi) dx_3, \quad (1)$$

$$\mu(x_3, x_3 + \xi) = \frac{\langle p^*(x_3)p(x_3 + \xi) \rangle}{\sqrt{\langle |p(x_3)|^2 \rangle} \sqrt{\langle |p(x_3 + \xi)|^2 \rangle}} \quad (2)$$

where $\gamma(\xi)$ denotes spanwise averaged coherence function of the surface pressure, $p(x_3)$ and $p(x_3 + \xi)$ denotes surface pressure on the body at spanwise coordinate x_3 and $x_3 + \xi$ respectively, a denotes computational or measured span and $\langle \rangle$ denotes ensemble averaging.

The coherent length l is defined to be the value taken such that a Gaussian function which includes l as parameter like following is best curve-fitted to computed or measured $\gamma(\xi)$ using a nonlinear least-square method, namely

$$\text{Re}(\gamma) \approx e^{-\frac{\xi^2}{2l^2}}. \quad (3)$$

2.2 Experimental Setup

The experimental setup around outlet of low-noise wind tunnel and details of the test body is shown in Fig. 1. As shown in Fig. 1b, 12 surface pressure sensing ports are holed on square cylindrical test body of side length $L = 14$ mm and length 500 mm. Pressure fluctuation in the ports are detected by embedded microphones and all pressure data are simultaneously recorded

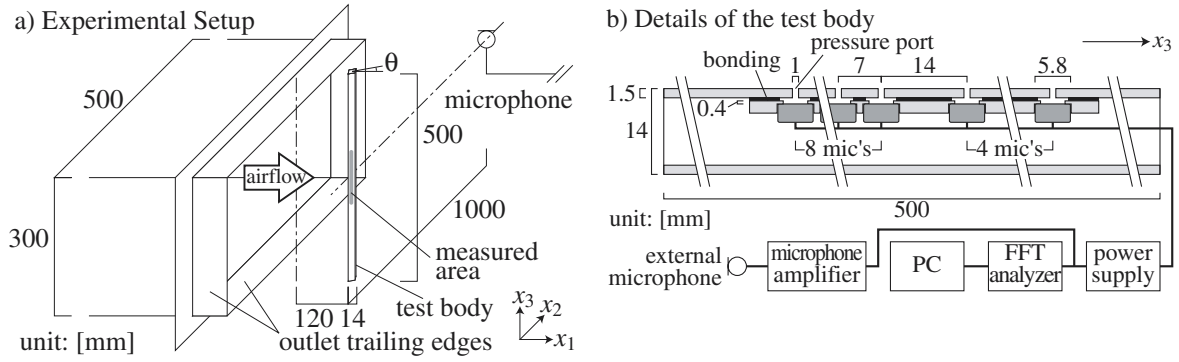


Figure 1: a) Experimental setup and b) details of the test body.

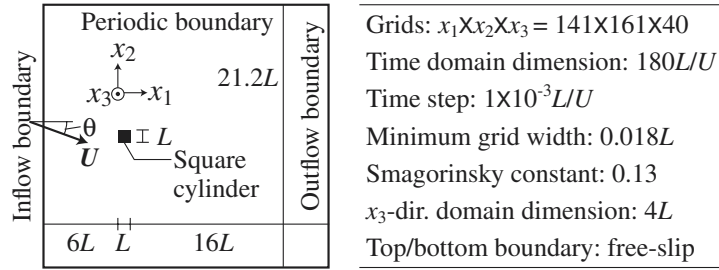


Figure 2: Geometry of computational domain (left) and computational conditions (right).

by the host PC. Integration in Eq. (1) was omitted in actual measurements assuming spatial stationarity in spanwise surface pressure distribution.

2.3 Numerical Methods

The incompressible Navier-Stokes equations are solved by three-dimensional large eddy simulation with the standard Smagorinsky subgrid-scale model adopted. Detailed numerical methods follow the reference [1]. Computational domain and conditions are shown in Fig. 2. Angle of attack θ of the body to mainstream is set by giving deflected mainstream velocity at the inflow boundary, because the body is fixed to the orthogonal computational grids. Ensemble averaging in Eq. (2) was omitted in actual computations assuming spatial ergodicity in spanwise pressure distribution.

2.4 Experimental and Computational Conditions

Detailed experimental and computational conditions and test case names are shown in Tab. 1. The mainstream velocities U are chosen to be from 5 to 10 m/s in measurements and fixed to 7 m/s in computations. The angles of attack θ are 0 and 30° . The frequency scales U/L and the Reynolds numbers R_e are also shown in the table.

Table 1: Experimental and computational conditions.

	experiment						simulation	
cases	5-0	5-30	7-0	7-30	10-0	10-30	s7-0	s7-30
θ [°]	0	30	0	30	0	30	0	30
U [m/s]	5.0		7.0		10.0		7.0	
U/L [1/s]	357		500		714		500	
Re [$\times 10^3$]	4.62		6.47		9.24		6.47	

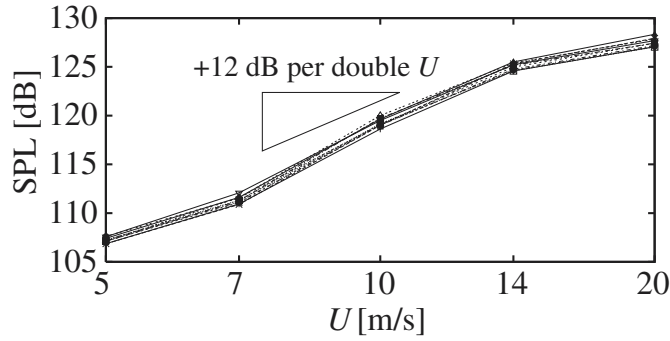


Figure 3: RMS values of surface pressure in SPL detected by each microphone.

3 RESULTS

3.1 Surface Pressure Power

Embedded microphone outputs must be confirmed not to be saturated by intense pressure fluctuations which could be over 100 dB in SPL. Fig. 3 shows the RMS values of surface pressure fluctuations detected by each of the microphones as functions of mainstream velocity U . Linear increases in SPL following the U^4 law (+12dB per double U) are observed until $U = 14$ m/s.

3.2 Coherence Functions

In Fig. 4, measured $\text{Re}(\gamma)$ are plotted against spanwise distance ξ/L and Strouhal number S_t . In all cases $\text{Re}(\gamma)$ decreases as ξ/L increases except at the Strouhal numbers corresponding to the Kármán vortex shedding, $S_{t,\text{peak}}$ where higher coherence is observed for all ranges of ξ/L . The distribution of the $\text{Re}(\gamma)$ is roughly identical in all cases, except for fluctuation in $S_{t,\text{peak}}$ and for slightly lower $\text{Re}(\gamma)$ at $S_{t,\text{peak}}$ in case 7-30 than in the other cases.

The computational results are shown in Fig. 5. The plotted regions of ξ/L are limited to $\xi/L \leq 3.9$ because the computational span is chosen to be $4L$ due to restriction in computational resources. In all cases, decrement in $\text{Re}(\gamma)$ is observed against increment in ξ/L until ξ/L reach around 2.0. On the contrary, in the region of $\xi/L > 2.0$, oscillation in $\text{Re}(\gamma)$ is observed because of reduction in number of spanwise averaging in Eq. (1). Strong coherences ($\text{Re}(\gamma) > 0.97$),

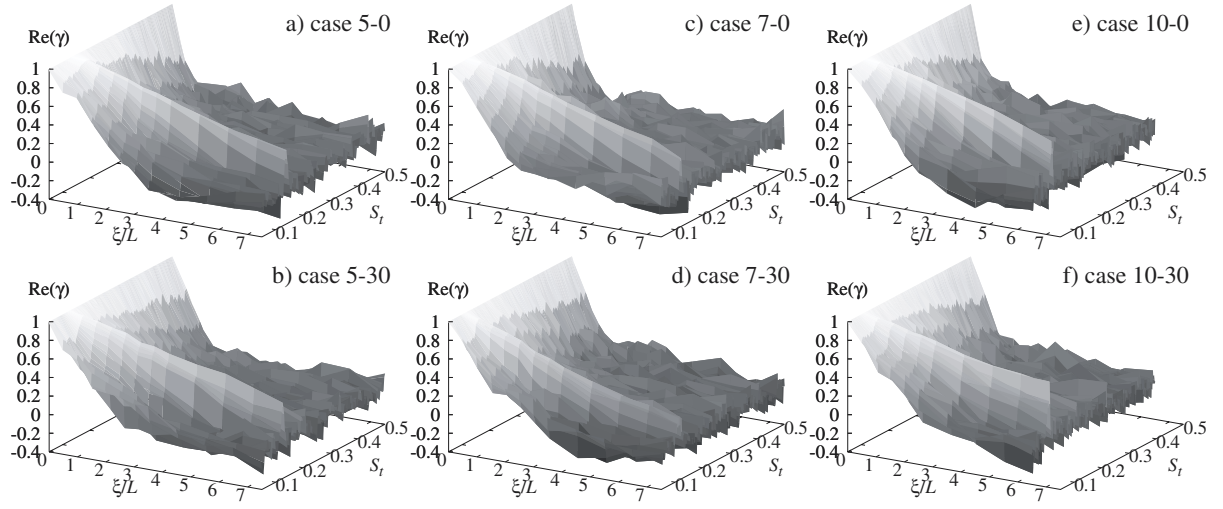


Figure 4: Measured $\text{Re}(\gamma)$ versus ξ/L and St .

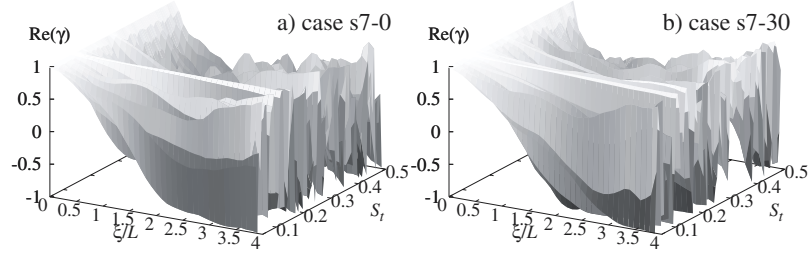


Figure 5: Computed $\text{Re}(\gamma)$ (note different scalings from Fig. 4).

however, are observed at the Kármán vortex shedding frequencies for all ranges of ξ/L .

In both Figs. 4 and 5, locally negative coherences are observed because only the real part of coherence is plotted, which are especially clearly seen in Fig. 5.

3.3 Coherent Lengths

Fig. 6 shows coherent length l obtained by curve-fitting a Gaussian function of the form shown in Eq. (3) to measured $\text{Re}(\gamma)$. The Strouhal numbers where l/L takes their maximums, $S_{t,\text{peak}}$, and the maximum values are shown in Fig. 8. $S_{t,\text{peak}}$ of the cases where $\theta = 0$ approximately agree with the peak Strouhal numbers of the lift coefficient shown in the reference [3], around 0.13, at corresponding Reynolds numbers. The values of l/L at $S_{t,\text{peak}}$ are roughly constant around 5.0 except in case 7-30, whereas $S_{t,\text{peak}}$ decreases when $\theta = 30^\circ$ compared to the cases of $\theta = 0$.

In computational results shown in Fig. 7, the qualitative characteristics are common to the measured results, especially that $S_{t,\text{peak}}$ and l/L decrease when $\theta = 30^\circ$. The values of $S_{t,\text{peak}}$, however, are about 15 percent higher and the maximum values of l/L are about three times

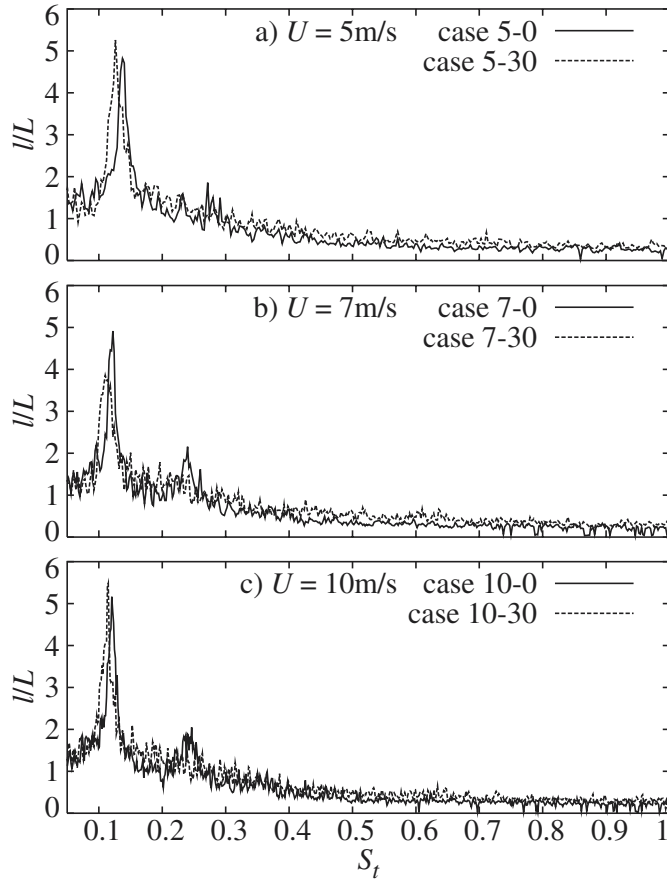


Figure 6: Measured coherent lengths.

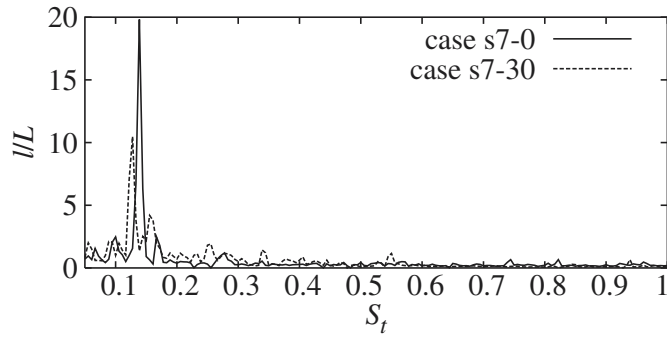


Figure 7: Computed coherent lengths.

higher than the measurements.

3.4 Conformity to Gaussian Functions

Fig. 8 shows measured $\text{Re}(\gamma)$ plotted against ξ/L at $S_t = S_{t,\text{peak}}$, $2S_{t,\text{peak}}$ and 0.5. The values of each Strouhal number, the estimated values of l/L which fit best to Gaussian functions Eq. (3)

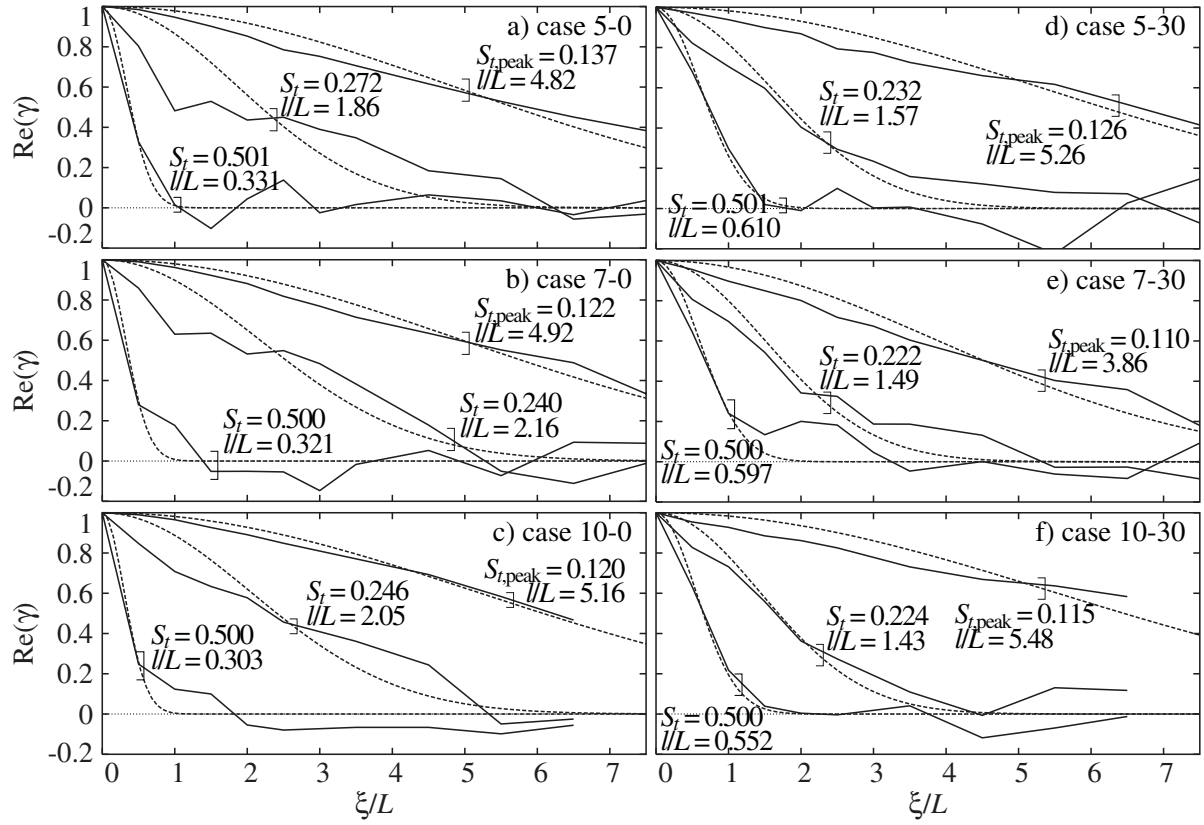


Figure 8: Measured $\text{Re}(\gamma)$ plotted against ξ/L at representative Strouhal numbers (solid lines) and their curve-fitted Gaussian functions (dashed lines). Estimated values of l/L are indicated in the figure.

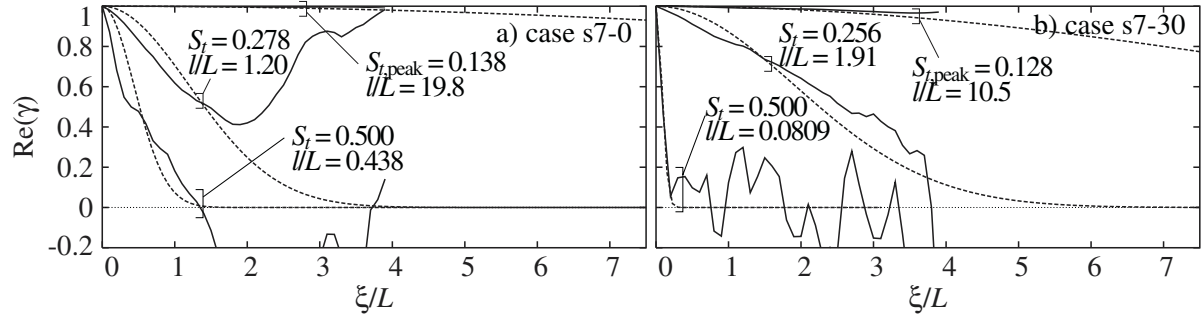


Figure 9: Computed $\text{Re}(\gamma)$ plotted against ξ/L at representative Strouhal numbers (solid lines) and their curve-fitted Gaussian functions (dashed lines). Estimated values of l/L are indicated in the figure. $\gamma(\xi)$ where $\xi/L \leq 2$ are used for curve-fitting.

and the curves of the functions are also shown in the figure. The estimated curves fit well with measured $\text{Re}(\gamma)$, except at $S_t = 2S_{t,\text{peak}}$ where moderate discrepancies are found. At $S_t = 0.5$, $|\text{Re}(\gamma)|$ is smaller than 0.2 when $\xi/L > 1$, which is considered to represent incoherency.

Computationally obtained $\text{Re}(\gamma)$ are shown in Fig. 9 with additional information following the measured results. Because of oscillation described above, only a portion of $\text{Re}(\gamma)$ where

$\xi/L \leq 2$ are used for curve-fitting. Although $\text{Re}(\gamma)$ fits well with a Gaussian function Eq. (3) when ξ/L is small, the oscillations causing discrepancy from the estimated curve are clearly observed except for the cases of $S_t = S_{t,\text{peak}}$. The values of l/L at $S_t = S_{t,\text{peak}}$ in cases 7-0 and s7-0 which became 4.92 and 19.8 respectively indicate much stronger coherence in computation than in measurement. Cases 7-30 and s7-30 follow the same tendency. The difference in approaching flow conditions that perfectly uniform inflow condition in computation compared to inevitably turbulent outlet airflow in measurement, could be considered as one of the causes of the discrepancy in coherence.

4 CONCLUSIONS

Spanwise spatial coherences of surface pressure on a square cylindrical body which acts as aerodynamic sound source are experimentally and computationally investigated in Reynolds numbers ranging from 4.62×10^3 to 9.24×10^3 and angle of attack from 0 to 30° . The results tell that the assumption of the real part of complex coherence of surface pressure as function of spanwise distance obeying a Gaussian function is proven to be generally reasonable, and that computationally estimated coherent lengths agreed with measurements in peak Strouhal numbers and in other qualitative characteristics. Peak values in computations, however, are estimated to be much higher than in measurements. The investigation of the cause remains to be a future work.

REFERENCES

1. T. Oshima et al., "Numerical prediction of aeroacoustic noise radiated from balusters of buildings with large eddy simulation", *Proc. Internoise 2000* (Nice), **4**, 2359–2362 (2000)
2. T. Oshima et al., "Numerical study on effect of inflow wind characteristics to generation of aeroacoustic noises from balusters of buildings", *Proc. Internoise 2001* (Hague), No. 511 (2001)
3. M. Shimizu et al., "Fluid forces working on rectangular-section cylindrical-shaped bodies, *J. of Japan Society of Mechanical Engineers* (Japanese), Part 2, **44**-384, 2699–2706 (1978)